Journal of Alloys and Compounds 685 (2016) 962–970

Contents lists available at ScienceDirect

Journal of Alloys and Compounds

journal homepage: http://www.elsevier.com/locate/jalcom

Structural and electrical study of the topological insulator $SnBi_2Te_4$ at high pressure

R. Vilaplana [a, *], J.A. Sans [b], F.J. Manjón [b], A. Andrada-Chacón [c], J. Sánchez-Benítez [c], C. Popescu [d], O. Gomis [a], A.L.J. Pereira [b], B. García-Domene [e], P. Rodríguez-Hernández [f], A. Muñoz [f], D. Daisenberger [g], O. Oeckler [h]

[a] Centro de Tecnologías Físicas, MALTA Consolider Team, Universitat Politècnica de València, Valencia, Spain
[b] Instituto de Diseño para la Fabricación y Producción Automatizada, MALTA Consolider Team, Universitat Politècnica de València, Valencia, Spain
[c] Departamento de Química-Física, MALTA Consolider Team, Universidad Complutense de Madrid, Madrid, Spain
[d] ALBA-CELLS, Barcelona, Spain
[e] Departamento de Física Aplicada-ICMUV, MALTA Consolider Team, Universidad de Valencia, Valencia, Spain
[f] Departamento de Física, Instituto de Materiales y Nanotecnología, MALTA Consolider Team, Universidad de La Laguna, Tenerife, Spain
[g] Diamond Light Source Ltd, Oxon, England, United Kingdom
[h] Institut für Mineralogie, Kristallographie und Materialwissenschaft, Universität Leipzig, Germany

ARTICLE INFO

Article history:
Received 20 April 2016
Received in revised form
16 June 2016
Accepted 17 June 2016
Available online 19 June 2016

Keywords:
High pressure
X-ray diffraction
Transport properties
Topological insulators
Electronic topological transition

ABSTRACT

We report high-pressure X-ray diffraction and electrical measurements of the topological insulator $SnBi_2Te_4$ at room temperature. The pressure dependence of the structural properties of the most stable phase of $SnBi_2Te_4$ at ambient conditions (trigonal phase) have been experimentally determined and compared with results of our *ab initio* calculations. Furthermore, a comparison of $SnBi_2Te_4$ with the parent compound Bi_2Te_3 shows that the central TeSnTe trilayer, which substitutes the Te layer at the center of the TeBiTeBiTe layers of Bi_2Te_3, plays a minor role in the compression of $SnBi_2Te_4$. Similar to Bi_2Te_3, our resistance measurements and electronic band structure simulations in $SnBi_2Te_4$ at high pressure suggest that this compound exhibits a pressure-induced electronic topological transition or Lifshitz transition between 3.5 and 5.0 GPa.

1. Introduction

Nowadays, Bi_2Te_3 is considered the best thermoelectric material at ambient temperature [1,2]. Numerous studies have been devoted to solid solutions of this material and related compounds, like other binary compounds as SnTe [1,3–9], in order to improve its thermoelectric properties. The number of studies of Bi_2Te_3 and related layered semiconductors has dramatically increased in the last years after the prediction and discovery of Bi_2Te_3, Bi_2Se_3, and Sb_2Te_3 as three-dimensional (3D) topological insulators (TIs). This discovery paved the way to search of new 3D-TIs in related materials with a view to future application [10–22]. In this regard, recent calculations and experiments of several ternary layered compounds of the AB_2Te_4 (A = Ge, Sn, Pb; B = Sb,Bi) family have been demonstrated to exhibit 3D-TI behavior, such as $SnBi_2Te_4$ [23–29].

Like the parent compound Bi_2Te_3, $SnBi_2Te_4$ crystallizes in a trigonal structure with space group (S.G.) $R\bar{3}m$ (Nº. 166, Z = 3), but with 4 atoms at independent positions (Sn at 3*a* Wyckoff sites and Bi, Te_1 and Te_2 at 6*c* Wyckoff sites) [3,6,30–34]. The hexagonal unit cell of Bi_2Te_3 contains three quintuple layer (QL) atomic blocks (Te_1–Bi–Te_2–Bi–Te_1), whereas the unit cell of $SnBi_2Te_4$ contains three septuple layer (SL) atomic blocks (idealized sequence: Te_1–Bi–Te_2–Sn–Te_2–Bi–Te_1). A view of the structures of Bi_2Te_3 and $SnBi_2Te_4$ with the hexagonal unit cell and a detail of the QL and SL are shown in Fig. 1(a) and (b), respectively. These structure drawings were done with VESTA code [35]. As can be observed, the difference between the structure of $SnBi_2Te_4$ and the structure of the binary parent compound Bi_2Te_3 is that the central Te_2 layer of the Bi_2Te_3 is replaced with a Te_2–Sn–Te_2 trilayer in $SnBi_2Te_4$. In both compounds, layers are piled up along [001] and are joined by weak van der Waals forces, while bonds inside the layers (extended

* Corresponding author. Departamento de Física Aplicada, Escuela Politécnica Superior de Alcoy, Universitat Politècnica de València, Placeta Ferràndiz i Carbonell 2, 03802, Alcoy, Alicante, Spain.
E-mail address: rovilap@fis.upv.es (R. Vilaplana).

http://dx.doi.org/10.1016/j.jallcom.2016.06.170
0925-8388/

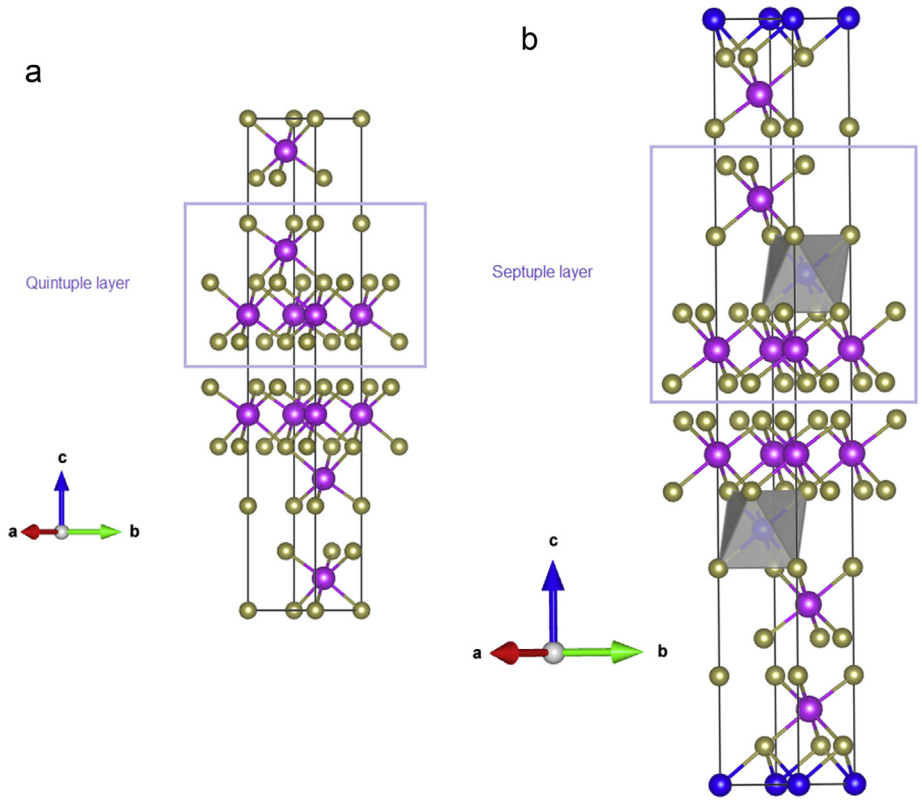

Fig. 1. (a) Bi_2Te_3 unit cell at ambient pressure with one QL highlighted. (b) SnB_2Te_4 unit cell at ambient pressure with one SL highlighted. Blue, magenta and brown colors correspond to Sn, Bi and Te atoms, respectively. (For interpretation of the references to color in this figure legend, the reader is referred to the web version of this article.)

in the (001) plane) have predominantly polar covalent character. In $SnBi_2Te_4$, the Sn atom is located at the center of an almost regular Te octahedron, while Bi is near the center of a distorted Te octahedron, like in Bi_2Te_3. Some experimental studies on $SnBi_2Te_4$ suggest that this compound exhibits a certain disorder in its crystalline structure due to mixed Sn/Bi occupancy of cationic sites [30,32]. However, other studies suggest that $SnBi_2Te_4$ has ordered SL atomic blocks [31,34].

To further understand the properties of this interesting compound, we report an experimental study of the structural and electrical properties of the most stable phase of $SnBi_2Te_4$ at ambient conditions by means of synchrotron-based X-ray diffraction (XRD) and electrical resistance measurements at high pressures (HP) up to 9 GPa. Additionally, *ab initio* simulations of structural parameters in ordered $SnBi_2Te_4$ at different pressures have been performed in order to compare them with experimental measurements. The main objective of this study is to characterize the structure of the low pressure phase of this compound under compression (with the aim to compare it with the behavior of its parent compound Bi_2Te_3) and to study the possible existence of a pressure-induced electronic topological transition (ETT) or Lifshitz transition in $SnBi_2Te_4$, as it occurs in Bi_2Te_3 and related compounds [36–47]. For this last purpose, we have carried out resistance measurements and theoretical electronic band structure simulations in $SnBi_2Te_4$ at different pressures, which have been analyzed in comparison to its parent compound Bi_2Te_3.

2. Experimental section

2.1. Sample preparation and characterization

Bulk samples of $SnBi_2Te_4$ were prepared by melting stoichiometric amounts of the pure elements Sn (99.999%, Smart Elements), Bi (99.999%, Smart Elements) and Te (99.999%, Alfa Aesar) at 890 °C for 4 h in sealed silica glass ampoules under argon atmosphere and subsequent annealing at 500 °C for 160 h, similarly to those of $SnSb_2Te_4$ [48]. Representative parts of the samples were crushed to powders and fixed on Mylar foils with hair-fixing spray to collect powder diffraction patterns on a Huber G670 powder diffractometer equipped with an image plate detector ($Cu–K_{\alpha 1}$ radiation, Ge (111) monochromator, $\lambda = 1.54051$ Å) in Guinier geometry. Rietveld refinement confirmed the high purity of the synthesized sample.

2.2. Measurements

Two powder angle-dispersive HP-XRD experiments at ambient temperature were carried out. The first one up to 37.2 GPa was conducted at beamline I15 of Diamond Light Source using a monochromatic X-ray beam ($\lambda = 0.42408$ Å). $SnBi_2Te_4$ powder and a strip of Cu were loaded in a 150-μm diameter hole of an Inconel gasket inside a membrane-type diamond-anvil cell (DAC) with diamond-culet sizes of 350 μm. He gas was used as pressure-transmitting medium. The X-ray beam was focused down to 70×70 μm^2 using Kickpatrick-Baez mirrors. A pinhole assembly placed before the sample position was used to collimate the beam down to 30 μm (round diameter) and as a clean-up aperture for filtering out the tail of the X-ray beam. Images were collected using a MAR345 image plate located at 430 mm from the sample. In order to obtain more data points of the low-pressure phase, a second HP-XRD experiment was conducted at beamline MSPD-BL04 [49] of ALBA Synchrotron Light Source using monochromatic radiation ($\lambda = 0.4246$ Å) up to 8 GPa. Silicon oil was used as a pressure-transmitting medium in this second experiment. In both experiments, pressure was determined using the copper equation of state (EOS) with parameters obtained by a Vinet equation [50].

Diffraction patterns were integrated as a function of 2θ using FIT2D in order to give conventional, one-dimensional diffraction profiles [51]. Indexing and Le Bail refinement in the powder diffraction patterns was performed using UNITCELL [52], POWDERCELL [53] and GSAS [54,55] program packages. Although the monochromatic radiation of both beamlines corresponds to Sn K-edge absorption, Rietveld refinements taking into account resonant X-ray diffraction were not successful due to pronounced preferred orientation. Consequently, we have performed Le Bail fitting which allows refining unit cell parameters but not atomic positions.

Electrical resistance measurements at HP were performed by using the standard four-point probe van der Pauw method [56] in a modified Merrill-Bassett-type DAC with 400 μm culet diamonds. Thin flakes approximately 30 μm thick and with a 100 × 100 μm^2 surface for the measurements were obtained from cleaving the original single crystals. As the accurate measurement of the sample dimensions (thickness and the distance between the four electrodes inside the DAC) was impossible, the resistivity could not be calculated. The electrical resistance was measured using four 20 μm-thick copper–beryllium wires in two different arrangements: in the first one, samples were placed directly between the anvils without any pressure transmitting medium; i.e., under uniaxial conditions. In the second one, measurements were performed under quasi-hydrostatic conditions by using stainless steel gaskets and CsI powder as a pressure transmitting medium. In both arrangements the luminescence of ruby powder was used to determine pressure [57,58]. In both setups, measurements were conducted up to 10 GPa and the R_1 and R_2 ruby lines remained well resolved to obtain accurately the pressure in the whole pressure range. In the two experiments, the electrical resistance showed similar trends, probably due to the anisotropic (layered) and soft nature of the crystals.

3. Theoretical calculations

Ab initio total-energy calculations were carried out for $SnBi_2Te_4$ in the low-pressure trigonal $R\bar{3}m$ structure without considering disorder. They were performed within the density functional theory (DFT) [59] using the plane-wave method and the pseudopotential theory with the Vienna Ab initio Simulation Package (VASP) [60,61]. The projector-augmented wave scheme (PAW) [62] was used as implemented in this package and the basis set of plane waves extended up to an energy cutoff of 320 eV to achieve highly converged results and accurate description of the electronic properties. Bi semicore *d* orbitals were included within a scalar relativistic scheme to take into account the spin-orbit interaction (SOI). The exchange-correlation energy was described in the generalized gradient approximation (GGA) with the PBEsol [63] prescription. In order to obtain very well converged energies and forces, a 6 × 6 × 6 grid of special k-points was employed for the integration over the Brillouin zone (BZ). At selected volumes, the structures were fully relaxed to their optimized configuration through the calculation of the forces on atoms and the stress tensor. In the optimized configurations, the forces on the atoms were less than 0.002 eV/Å and the deviations of the stress tensor from a diagonal hydrostatic form are smaller than 1 kbar (0.1 GPa). The electronic band structures along high symmetry directions and the corresponding density of states (DOS) were calculated with a mesh of 18 × 18 × 18 k-points.

4. Results and discussion

As mentioned previously, $SnBi_2Te_4$ is a layered structure composed of SL atomic blocks piled along the hexagonal *c* axis and joined by weak van der Waals forces. The XRD pattern of $SnBi_2Te_4$ at ambient conditions is shown in Fig. 2. Le Bail refinement yielded

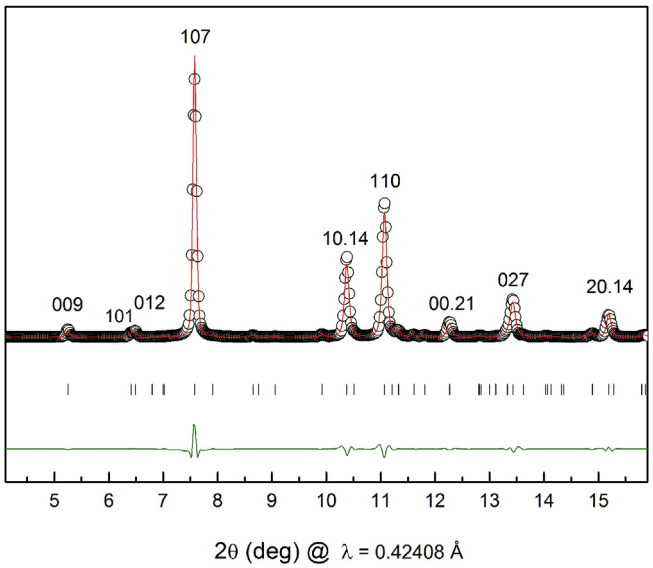

Fig. 2. Powder XRD pattern of $SnBi_2Te_4$ at ambient pressure (open symbols). Le Bail refinement (solid red line) and residuals are also plotted. Tick marks correspond to $SnBi_2Te_4$ reflections of the trigonal phase. (For interpretation of the references to color in this figure legend, the reader is referred to the web version of this article.)

the following hexagonal lattice parameters at ambient pressure: a = 4.40283 (10) Å, c = 41.7139 (22) Å, resulting in a volume of V_0 = 700.28 (6) $Å^3$. Rietveld refinement of resonant XRD data in comparable as-grown samples of $SnSb_2Te_4$ revealed the presence of some cation disorder [48], which is also expected in $SnBi_2Te_4$. However, since Rietveld refinement proved impossible in this work, we cannot discuss the evolution of disorder with pressure in $SnBi_2Te_4$. In this respect, it must be noted that the lattice parameters obtained by Le Bail refinement show good agreement with our theoretical ones that do not consider disorder (see Table 1) and with experimental ones previously reported [3,6,8,29,30,32,33]. Furthermore, our theoretical values also compare well to previously reported calculations [29]. For the sake of completeness, our theoretical fractional atomic coordinates for the trigonal phase of $SnBi_2Te_4$ at ambient conditions are reported in Table 2.

Fig. 3 shows powder HP-XRD patterns of $SnBi_2Te_4$ at selected pressures up to 7.9 GPa. New reflections (see asterisks in Fig. 3) appear at 7 GPa and increase at higher pressure, thus indicating a phase transition that is reversible after decreasing pressure from

Table 1
Experimental (Exp) and theoretical (The) lattice parameters and volume corresponding to the trigonal phase of $SnBi_2Te_4$ at ambient conditions.

a (Å)	c (Å)	V_0 ($Å^3$)	Ref.
4.40283 (10)	41.7139 (22)	700.28 (6)	Exp[a]
4.411	41.511	699.468	Exp[b]
4.3954 (4)	41.606 (1)	696.119	Exp[c]
4.404 (1)	41.612 (5)	698.946	Exp[d]
4.405 (1)	41.60 (1)	699.062	Exp[e]
4.40387 (3)	41.6003 (4)	698.708	Exp[f]
4.3915	41.1948	688.016	The[a,*]
4.39	41.61	694.476	The[g,*]

*All calculations include SOI.
[a] This work.
[b] Ref. [30].
[c] Ref. [32].
[d] Ref. [3].
[e] Refs. [33] and [6].
[f] Ref. [8].
[g] Ref. [29].

Table 2
Theoretical atomic positions corresponding to the trigonal phase of $SnBi_2Te_4$ at zero pressure.

Atoms	Sites	x	y	z
Sn	3a	0	0	0
Bi	6c	0	0	0.4268
Te_1	6c	0	0	0.1349
Te_2	6c	0	0	0.2890

8 GPa (see pattern of the recovered sample at 2.4 GPa on top of Fig. 3). We want to comment that the discussion of the structure of the high-pressure phase of $SnBi_2Te_4$ above 7 GPa is out of the scope of the present work and will be reported elsewhere.

The pressure dependence of the unit cell volume of $SnBi_2Te_4$ is shown in Fig. 4. Full and open red circles represent the measurements carried out in the first and the second experiment, respectively. The bulk modulus of $SnBi_2Te_4$ has been characterized using a third-order Birch–Murnaghan equation of state (BM–EOS) [64]. Table 3 shows the experimental and theoretical values of the unit cell volume, bulk modulus and its pressure derivative at ambient

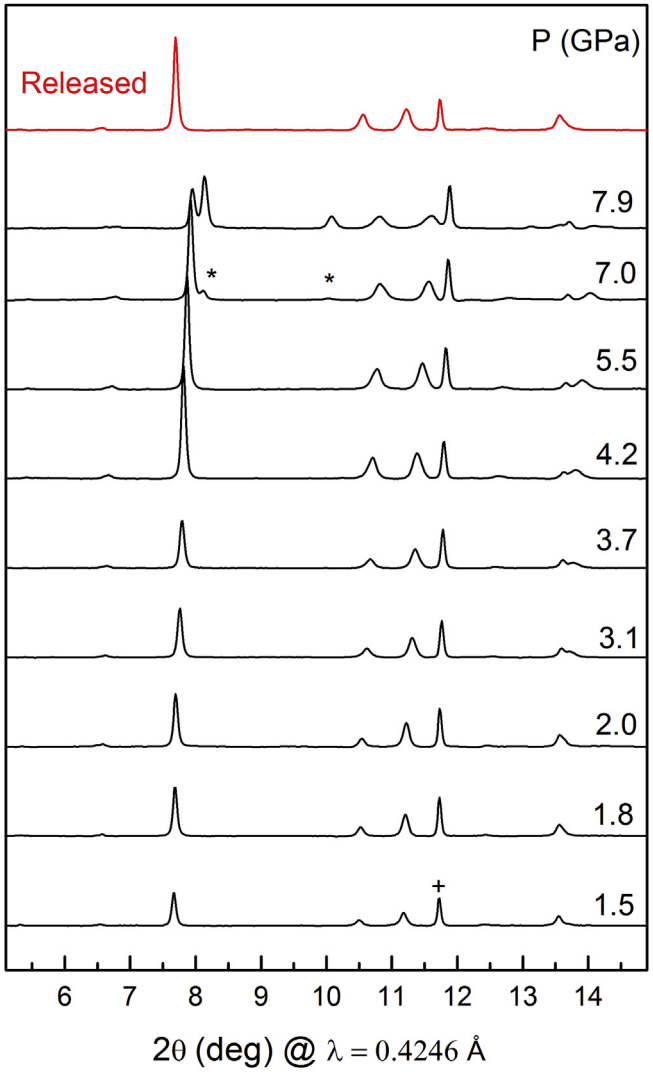

Fig. 3. Powder XRD patterns of $SnBi_2Te_4$ at selected pressures up to 7.9 GPa. Patterns shifted along vertical axis for comparison. Asterisks indicate reflections of the new phase and the plus symbol represents the (111) copper Bragg reflection. The pattern of $SnBi_2Te_4$ at 2.4 GPa on decreasing pressure is shown at the top.

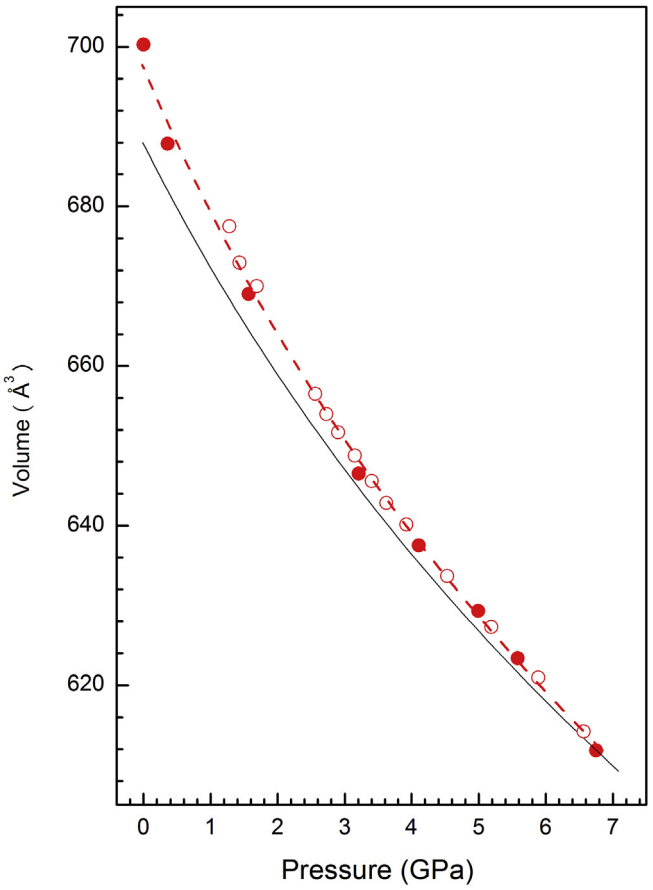

Fig. 4. Experimental (symbols) and theoretical (solid lines) pressure dependence of the unit-cell volume of $SnBi_2Te_4$ under compression. Experimental data are fit to a third-order BM–EOS (dashed lines). Full and open circles represent the measurements carried out at Diamond and Alba synchrotron facilities, respectively.

Table 3
Experimental (Exp) and theoretical (The) parameters of the third-order BM–EOS of $SnBi_2Te_4$ and Bi_2Te_3 at ambient conditions: volume (V_0), bulk modulus (B_0), and its pressure derivative (B_0').

Compound	V_0 (Å^3)	B_0 (GPa)	B_0'	Character
$SnBi_2Te_4$	697.8 (1)	35 (2)	6.2 (7)	Exp[a]
	688.0 (5)	41.1 (9)	5.8 (3)	The[a]
Bi_2Te_3	507.6	56.2	2.1	Exp[b]
		21.9*	17.1	Exp[c]
		38.2†	4.6	
	505.1	35.1‡	6.2	Exp[d]
	510.4	46.3	3.6	Exp[e]
		50.1	3.0	
		32.5	10.1	Exp[f]
	500.0	41.6	4.68	The[g]
		28.1		The[h]
		40.3		The[i]

* Below 2 GPa, † above 2 GPa, ‡ whole pressure range.
[a] This work.
[b] Ref. [39].
[c] Ref. [44].
[d] Ref. [45].
[e] Ref. [65].
[f] Ref. [66].
[g] Ref. [41].
[h] Ref. [46].
[i] Ref. [67].

pressure for $SnBi_2Te_4$. Values for Bi_2Te_3 have also been added for comparison. Experimental values for $SnBi_2Te_4$ are in good agreement with theoretical calculations and the bulk modulus has a similar value in both $SnBi_2Te_4$ and Bi_2Te_3. This result suggests that the Sn octahedrons in the center of the SLs do not play an important role in the resistance of $SnBi_2Te_4$ to compression at low pressures. Moreover, this result is consistent with what is expected for the layered structure of both compounds since the large compressibility of both semiconductors at room pressure is determined by the weak van der Waals forces between multiple adjacent layers piled up along the *c* axis.

The evolution of the lattice parameters under pressure is displayed in Fig. 5. In order to obtain the experimental and theoretical axial compressibilities of the *a* and *c* axes, we have fitted the lattice parameters obtained by Le Bail fitting and by *ab initio* calculations to a modified Murnaghan EOS [68]. The axial bulk modulus B_{0i} obtained for each lattice parameter *i* allows us to determine the axial compressibility as $\kappa_i = 1/3B_{0i}$. Table 4 shows the experimental and theoretical results of the *a* and *c* axial bulk moduli and compressibilities in $SnBi_2Te_4$ and their comparison to Bi_2Te_3. The axial compressibility of the *c* axis is almost twice that of the *a* axis in $SnBi_2Te_4$. The same result is observed in Bi_2Te_3. Furthermore, the axial bulk moduli are similar, but slightly larger, in $SnBi_2Te_4$ than in Bi_2Te_3. Since the different bulk moduli fall within the experimental and theoretical uncertainties, it is difficult to ascertain whether this result is due to the substitution of the central Te layer in Bi_2Te_3 by the TeSnTe layer in $SnBi_2Te_4$. Finally, it is worth to mention that a minimum occurs between 3 and 4 GPa in the *c/a* ratio of our experimental and theoretical data for $SnBi_2Te_4$ (see inset in Fig. 5), as it was previously reported for Bi_2Te_3 [44,45].

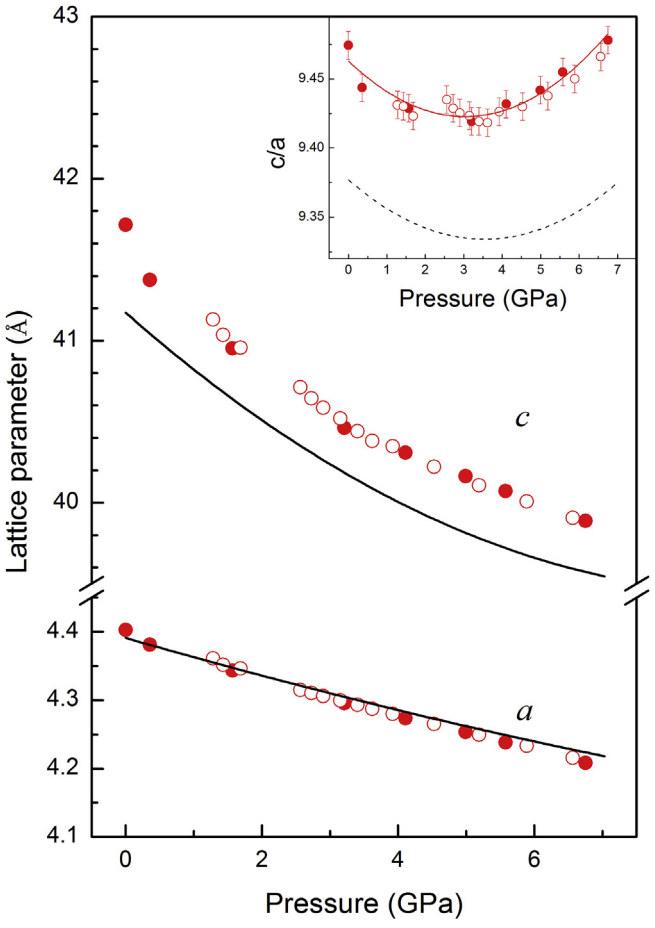

Fig. 5. Experimental (symbols) and (solid lines) pressure dependence of the lattice parameters of $SnBi_2Te_4$ under compression. Full and open circles represent the measurements carried out at Diamond and Alba synchrotron facilities, respectively. Inset shows the experimental (symbols) and theoretical (dashed line) pressure dependence of the axial *c/a* ratio. Solid red line represents the fit of experimental data. (For interpretation of the references to color in this figure legend, the reader is referred to the web version of this article.)

In order to better understand the structural behavior of $SnBi_2Te_4$ under compression we have plotted in Fig. 6 the pressure dependence of the theoretical interlayer Te_1Te_1 distance along the c-axis and intralayer Te_1Bi, Te_2Bi and Te_2Sn distances inside the SL. These distances show the pressure evolution of the irregular Bi and quasi-regular Sn octahedra, respectively. It can be clearly observed that the quasi-regular Sn octahedron (note that all SnTe distances are equal but the TeSnTe angles are slightly different from 90°) is slightly compressed as indicated by the decrease of the Te_2Sn distance. On the other hand, the distorted Bi octahedron is not so much compressed (Te_2Bi distance decreases while Te_1Bi bond distance increases) and tends to become more regular on increasing pressure. In any case, most of the compression of the trigonal phase at low pressure is clearly related to the strong decrease of the Te_1Te_1 interlayer distance with pressure, especially below 4 GPa. The change in the slope of the interlayer distance above 4 GPa is related to the strengthening of van der Waals interactions at high pressure as observed in many layered and molecular compounds [69,70]. Fig. 6 also shows the pressure dependence of the theoretical interlayer Te_1Te_1 distance along [001] and intralayer Te_1Bi, and Te_2Bi distances inside the QL of the parent compound Bi_2Te_3 taken from a previous calculation [41]. It can be observed that our calculations indicate that the Bi octahedron is slightly more compressed in $SnBi_2Te_4$ than in Bi_2Te_3. (Te_2Bi starts at the same but has steeper slope and ends at a smaller value and Te_1Bi seems parallel between the two compounds). Therefore, the structural differences between both compounds under compression are mainly related to the Sn octahedron and to a lesser extent to the Bi octahedron.

All the above mentioned results suggest that it is likely that $SnBi_2Te_4$ shows a pressure-induced ETT before undergoing a structural phase transition, just like it occurs in Bi_2Te_3 around 3–4 GPa [36,38,39,41,44–47]. The ETT is an isostructural transition of $2^{1/2}$ order which shows no volume discontinuity, where the Wyckoff positions of atoms are not modified during the transition. Since there is neither associated volume collapse during the transition nor change of the symmetry of the atomic positions, it is difficult to detect by XRD measurements. The ETT is a consequence of a topological change in the Fermi surface related to the passage of an extremum of the electron energy band (equivalent to the van Hove peak in the density of states) through the Fermi level. Apart from the direct observation of the changes at the Fermi surface by means of angle-resolved photoelectron spectroscopy, transport measurements have also been used as one of the most convincing ways to detect ETTs [36,38,39,47]. However, other transport properties such as electrical and thermal resistances, and the thermal expansion coefficient, could also provide subtle evidences for ETTs, as discussed by Kechin et al. [71] for Zn. In this regard, we have carried out resistance measurements complemented with electronic band structure calculations in order to shed some light into the possible pressure-driven ETT in $SnBi_2Te_4$.

Fig. 7 shows the resistance of $SnBi_2Te_4$ as measured during loading and unloading process up to and from 9.0 GPa (with CsI as pressure-transmitting medium). As can be observed, an increase of the resistance occurs between 3.5 and 5.0 GPa, not far from the minimum in the *c/a* ratio of our experimental and theoretical data for $SnBi_2Te_4$. Note that an increase in resistance was also observed previously in other ETT studies [72]. This result suggests that in $SnBi_2Te_4$, a pressure-induced ETT could occur during this pressure

Table 4
Experimental (Exp) and theoretical (The) and bulk moduli (B_0) of the lattice parameters of $SnBi_2Te_4$ and their associated axial compressibilities associated. Same information for Bi_2Te_3 is provided for comparison.

Material	B_{0a} (GPa)	B_{0c} (GPa)	κ_a (10^{-3} GPa^{-1})	κ_c (10^{-3} GPa^{-1})	Ref.
$SnBi_2Te_4$	42.3 (1.7)	25.3 (1.7)	7.9 (3)	13.1 (9)	Exp.[a]
	48.0 (1.4)	30 (2)	6.9 (7)	11.1 (7)	The (GGA-PBEsol)[a]
Bi_2Te_3	39.9 (1.5)	21.9 (1.2)	8.4 (3)	15.2 (8)	Exp.[b]
	46.1 (6)	29 (3)	7.2 (1)	11.6 (1.2)	The (GGA-PBEsol)[c]

[a] This work. Calculations including SOI.
[b] Ref. [45].
[c] Ref. [41].

interval, similar to the parent compound Bi_2Te_3 where changes around 3–4 GPa were observed before the first-order phase transition above 8.0 GPa [36,38,39,41,44–47]. On the other hand, a decrease of the resistance with pressure takes place between 7 and 8 GPa, which must be related to the high pressure phase evidenced by XRD measurements above 7 GPa. Finally, we have to note that the resistance recovers with some hysteresis when pressure is released, thus indicating that the phase transition above 7 GPa in $SnBi_2Te_4$ is reversible, as it was also recently observed in Bi_2Te_3 [73].

In order support the observation of a possible pressure-induced ETT in $SnBi_2Te_4$, we have performed electronic band structure calculations at different pressures (see Fig. 8) and have compared them with those of Bi_2Te_3 [41] (see Fig. 9). The calculations show that $SnBi_2Te_4$ is an indirect semiconductor at 0 GPa (with a narrow energy bandgap around 0.1 eV) which has the valence band maximum (VBM) along the L–Z direction (V_1) and the conduction band minimum (CBM) along the Γ–Z direction (C_1). Close in energy to these extrema, our calculations show a second VBM along the Z–F direction (V_2) and a second CBM along the F–Γ direction (C_2). Finally, our calculations predict the closing of the bandgap of the R-3m phase above 6 GPa, however due to the underestimation of the bandgap in DFT calculations it is expected that the real closure of the bandgap takes place above 7–8 GPa.

According to recent transport measurements at ambient conditions, $SnBi_2Te_4$ is prone to be an extrinsic p-type semiconductor with up to 10^{20} holes/cm^3 due to off-stoichiometry defects [74]. In our calculations for a pure intrinsic semiconductor, the VBM is taken as a reference energy (0 eV), so in a highly-doped semiconductor, the Fermi level must be well inside the valence band as shown in Fig. 8 by the dashed red line. At ambient pressure, it can be thought that the Fermi level is located between V_1 and V_2. However, as pressure increases, the difference in energy between V_1 and V_2 decreases so the Fermi level can cross V_2 (see Fig. 8 at 3.9 GPa) and cause a pressure-induced ETT in $SnBi_2Te_4$, which would explain the change observed in resistance above 3.5 GPa.

In a recent study of Bi_2Te_3, a similar reasoning was used to explain the observed pressure-induced ETT [46]. Calculations of our previous study of Bi_2Te_3 are in agreement with this recent work. Fig. 9 shows our calculated electronic band structure of Bi_2Te_3 at different pressures. In good agreement with the recent calculations [46], two VBMs (V_1 and V_2) very close in energy are observed at 0 GPa along the L–Z and Z–F directions; however, as pressure increases both VBM tend to separate in energy. Therefore, taking into account that Bi_2Te_3 is also a p-type semiconductor it is conceivable that both VBM are above the Fermi level (red dashed line in Fig. 9)

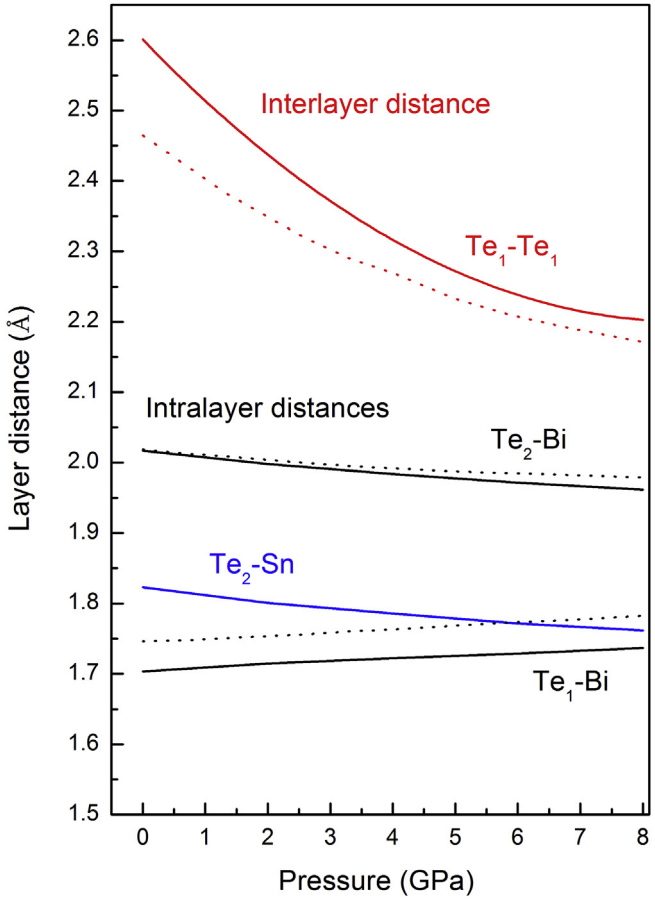

Fig. 6. Pressure dependence of the interlayer Te_1Te_1 and intralayer $BiTe_1$, $BiTe_2$ and $SnTe_2$ distances of $SnBi_2Te_4$ (solid lines) and Bi_2Te_3 (dotted lines) obtained from *ab initio* calculations.

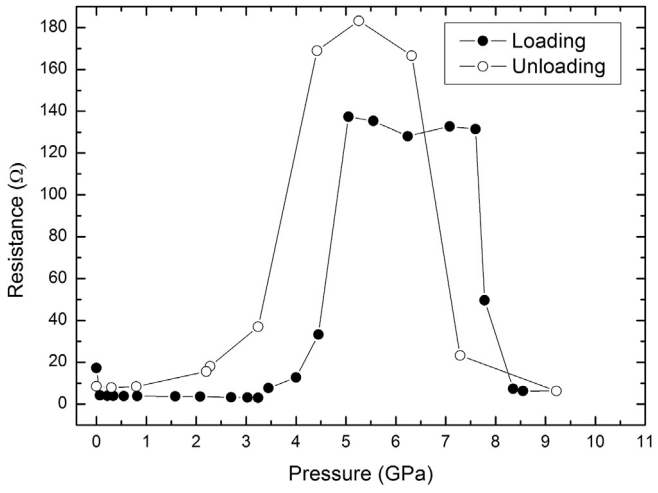

Fig. 7. Pressure dependence of the resistance of $SnBi_2Te_4$ recorded during loading (filled symbols) and unloading (empty symbols).

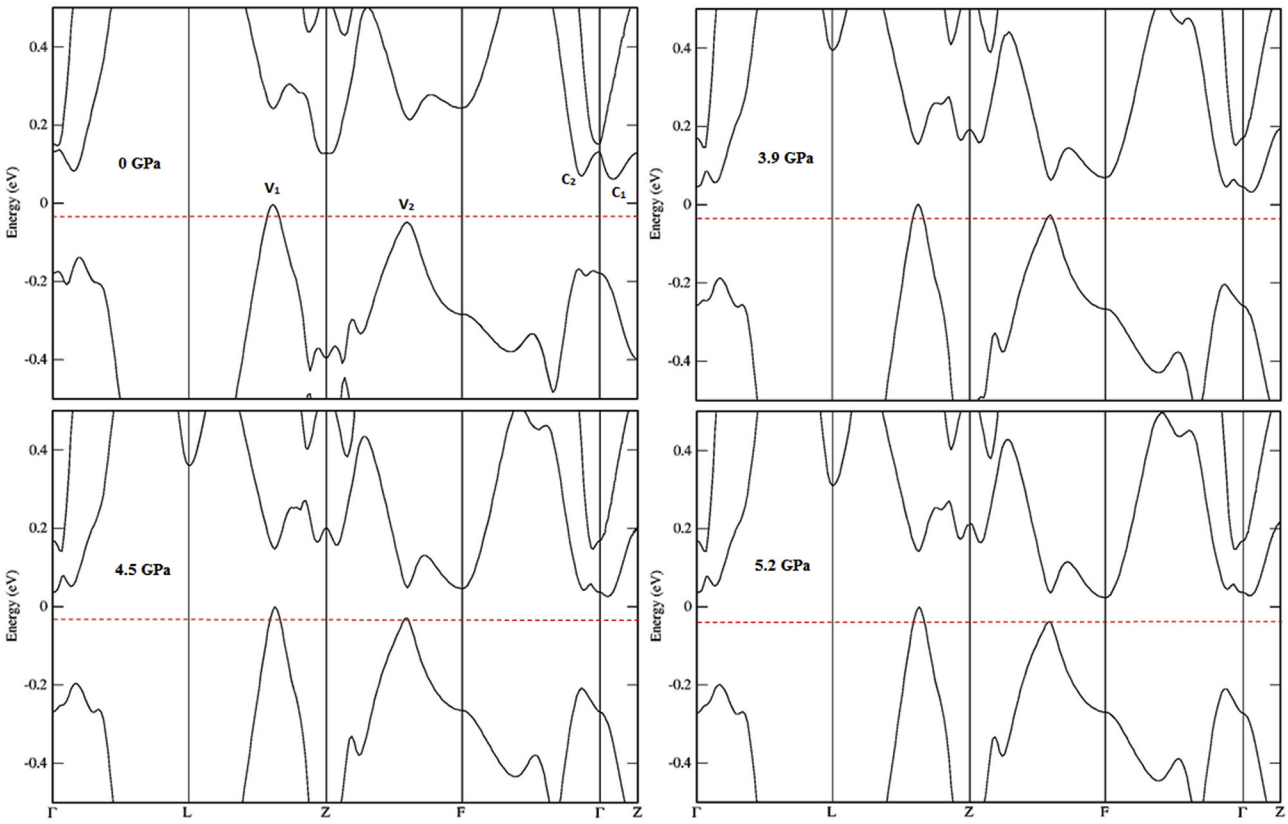

Fig. 8. Calculated electronic band structure of $SnBi_2Te_4$ at 0, 3.9, 4.5 and 5.2 GPa. Reference energy (0 eV) has been taken as the maximum of the valence band. A tentative position of the Fermi level in a highly-doped p-type sample is indicated by the horizontal red dashed line. (For interpretation of the references to color in this figure legend, the reader is referred to the web version of this article.)

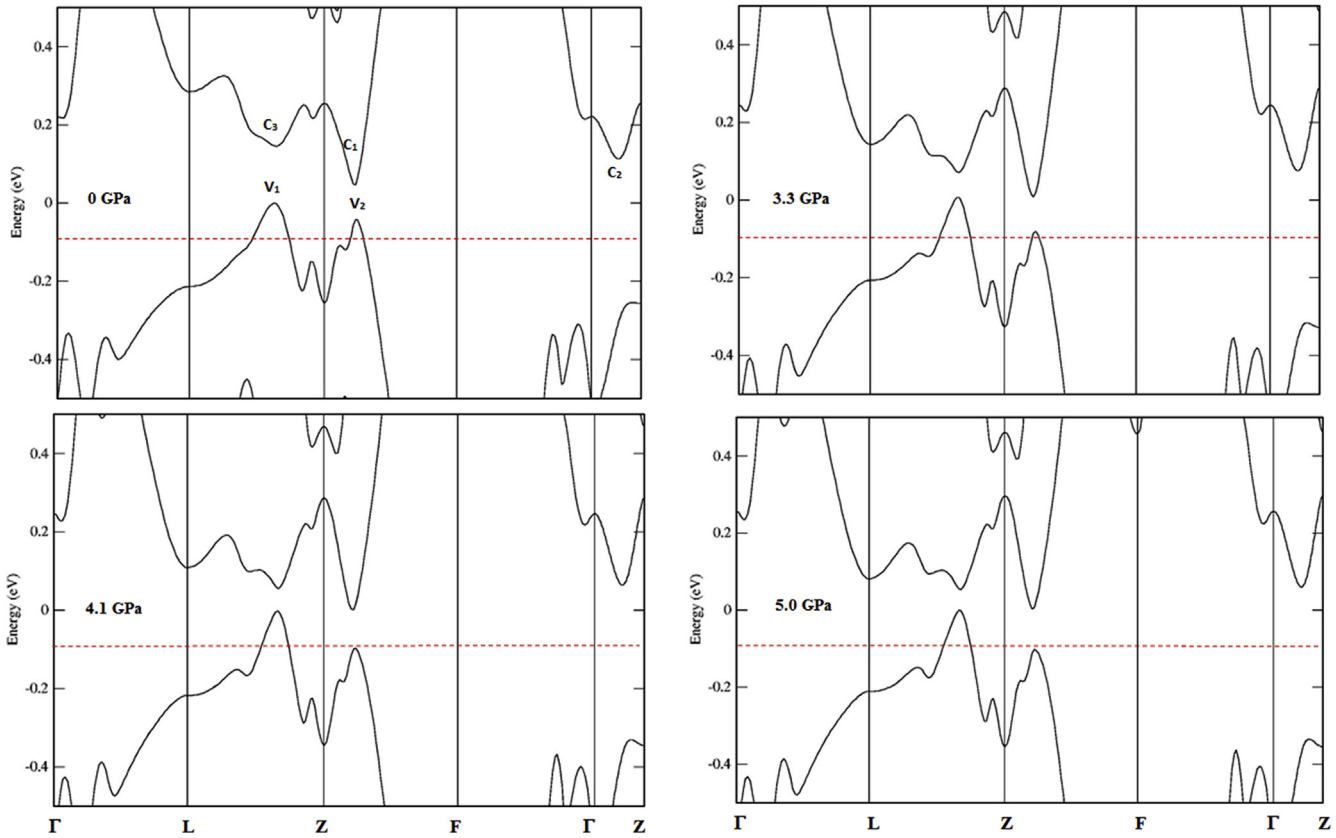

Fig. 9. Calculated electronic band structure of Bi_2Te_3 at 0, 3.3, 4.1 and 5.0 GPa. Reference energy (0 eV) has been taken as the maximum of the valence band. A tentative position of the Fermi level in a highly-doped p-type sample is indicated by the horizontal red dashed line. (For interpretation of the references to color in this figure legend, the reader is referred to the web version of this article.)

at low pressures; however, it is expected that the V_2 VBM cross below the Fermi level at high pressures, between 2 and 4 GPa depending on the hole concentration. This fact is responsible for the pressure-induced ETT observed in Bi_2Te_3. These theoretical results on Bi_2Te_3 give us confidence about our present calculations for $SnBi_2Te_4$.

In this way, we can explain the changes in the resistance with increasing pressure in $SnBi_2Te_4$ on the light of our theoretical calculations. As noted in Fig. 7, there is a rather symmetric resistance–pressure dependence below and above 6 GPa in $SnBi_2Te_4$. The explanation for this symmetric behavior is because the phases prior to 4 GPa and above 8 GPa show metallic-like character. Below 4 GPa, $SnBi_2Te_4$ is a low-bandgap semiconductor which shows metallic-like properties due to a high 3D hole concentration caused by non-stoichiometry defects. Note that the metallic-like behavior of low-bandgap semiconductors behaving as 3D-TIs due to their high 3D carrier concentration has been already discussed for Bi_2Se_3 [75]. On the other hand, our calculations allow us to conclude that the closing of the bandgap of the R-3m phase takes place above 7–8 GPa. Coincidentally, our XRD measurements show a structural phase transition above 7 GPa, likely to a metallic phase like in Bi_2Te_3 [47,76]. Both facts lead to a metallic behavior in $SnBi_2Te_4$ above 8 GPa. Therefore, it is clear that the conductivity below 4 GPa and above 8 GPa must have similar metallic-like features. As regards, the origin of the high resistance state between 4 and 8 GPa, we can explain it as due to the occurrence of a pressure-induced ETT caused by the crossing of the Fermi level by the VBM V_2. In this way, the redistribution of holes above 4 GPa between both VBM V_1 and V_2 leads to an increase in the resistivity of the material since holes at V_2 have a larger effective mass than holes at V_1. In summary, our theoretical simulations give support to a possible pressure-induced ETT between 3.5 and 5 GPa in $SnBi_2Te_4$. This pressure range for the ETT is consistent with the pressure at which we observed an increase of resistance.

5. Concluding remarks

We have investigated the structural and electric properties of the trigonal phase of $SnBi_2Te_4$ as a function of pressure. A reversible phase transition is observed above 7.0 GPa in $SnBi_2Te_4$, as it was also observed in Bi_2Te_3. The bulk equation of state and the axial compressibilities at zero pressure of the low-pressure phase of $SnBi_2Te_4$ have been determined. By comparison with Bi_2Te_3, our data confirm that the presence of an additional central TeSnTe layer in $SnBi_2Te_4$ induces subtle differences in the pressure dependence of the structural parameters, but not on the transition pressure to the high-pressure phase in both compounds. Similar volume and axial bulk moduli have been obtained for both compounds and a minimum in the *c/a* ratio (around 3.5 GPa) is observed in $SnBi_2Te_4$, similar to that observed in Bi_2Te_3. Consequently, the Sn octahedron at the center of the layer seems to play a minor role in the compression of the low-pressure phase of $SnBi_2Te_4$ under quasi-hydrostatic conditions. Finally, our high-pressure resistance measurements in $SnBi_2Te_4$ show an increase of resistance between 3.5 and 5.0 GPa not far from pressure where the minimum in the *c/a* ratio occurs. These results suggest the existence of a pressure-induced ETT in $SnBi_2Te_4$ similar to what occurs in Bi_2Te_3 around 3–4 GPa. In this regard, additional high-pressure measurements, including Raman scattering and magneto-transport measurements, as well as additional calculations are underway in order to study in detail the presence of a pressure-induced ETT in $SnBi_2Te_4$.

Acknowledgments

We thank Dr. Philipp Urban for preparing the sample. This work has been performed under financial support from Spanish MINECO under projects MAT2013-46649-C4-2-P, MAT2015-71070-REDC and CTQ2015-67755-C2-1-R and from Spanish Ministerio de Educación, Cultura y Deporte as part of "Programa Campus de Excelencia Internacional/Programa de Valoración y Recursos Conjuntos de I + D + i VLC/CAMPUS" through projects SP20140701 and SP20140871. One of the experiments were performed at MSPD-BL04 beamline at ALBA Synchrotron with the collaboration of ALBA staff. J.A.S. thanks "Juan de la Cierva" fellowship program for funding. A.A.-C. and J.S.-B. are also grateful to Spanish MINECO for the FPI (BES-2013-066112) and Ramón y Cajal (RyC-2010-06276) fellowships. We acknowledge Diamond Light Source for time on beamline I15 under Proposal EE9102.

References

[1] D.M. Rowe, CRC Handbook of Thermoelectrics, CRC Press Inc., New York, 1995.
[2] R. Venkatasubramanian, E. Siivola, T. Colpitts, B. O'Quinn, Nature 413 (2001) 597.
[3] L.A. Kuznetsova, V.L. Kuznetsov, D.M. Rowe, J. Phys. Chem. Solids 61 (2000) 1269.
[4] X.-S. Zhou, Y. Deng, C.-W. Nan, Y.-H. Lin, J. Alloys Comp. 352 (2003) 328.
[5] X.-S. Zhou, Y. Deng, G.D. Wei, J. Liu, C.-W. Nan, Sci. China 46 (2003) 509.
[6] L.E. Shelimova, O.G. Karpinskii, P.P. Konstantinov, E.S. Avilov, M.A. Kretova, V.S. Zemskov, Inorg. Mater. 40 (2004) 451.
[7] G.J. Snyder, E.S. Toberer, Nat. Mater. 7 (2008) 105.
[8] B.A. Kuropatwa, H. Kleinke, Z. Anorg. Allg. Chem. 638 (2012) 2640.
[9] L. Pan, J. Li, D. Berardan, N. Dragoe, J. Solid State Chem. 225 (2015) 168.
[10] L. Fu, C.L. Kane, Phys. Rev. B 76 (2007) 045302.
[11] L. Fu, C.L. Kane, E.J. Mele, Phys. Rev. Lett. 98 (2007) 106803.
[12] J.C.Y. Teo, L. Fu, C.L. Kane, Phys. Rev. B 78 (2008) 045426.
[13] X.-L. Qi, T.L. Hughes, S.C. Zhang, Phys. Rev. B 78 (2008) 195424.
[14] Y. Xia, D. Qian, D. Hsieh, L. Wray, A. Pal, H. Lin, A. Bansil, D. Grauer, Y.S. Hor, R.J. Cava, M.Z. Hasan, Nat. Phys. 5 (2009) 398.
[15] H. Zhang, C.X. Liu, X.L. Qi, X. Dai, Z. Fang, S.C. Zhang, Nat. Phys. 5 (2009) 438.
[16] Y.L. Chen, J.G. Analytis, J.H. Chu, Z.K. Liu, S.K. Mo, X.L. Qi, H.J. Zhang, D.H. Lu, X. Dai, Z. Fang, S.C. Zhang, I.R. Fisher, Z. Hussain, Z.X. Shen, Science 325 (2009) 178.
[17] D. Hsieh, et al., Phys. Rev. Lett. 103 (2009) 146401.
[18] J.E. Moore, Nature 464 (2010) 194.
[19] M.Z. Hasan, C.L. Kane, Rev. Mod. Phys. 82 (2010) 3045.
[20] L. Fu, Phys. Rev. Lett. 106 (2011) 106802.
[21] T.V. Menshchikova, S.V. Eremeev, E.V. Chulkov, JETP Lett. 94 (2011) 106.
[22] S.V. Eremeev, G. Landolt, T.V. Menshchikova, Z.S. Aliev, M.B. Babanly, J. Henk, A. Ernst, L. Patthey, A. Eich, A.A. Khajetoorians, J. Hagemeister, O. Pietzsch, J. Wiebe, R. Wiesendanger, P.M. Echenique, S.S. Tsirkin, I.R. Amiraslanov, J.H. Dil, E.V. Chulkov, Nat. Commun. 3 (2012) 635.
[23] S.Y. Xu, et al., arXiv:1007.5111 (2010).
[24] S.V. Eremeev, et al., Nat. Commun. 3 (2012) 635.
[25] K. Kuroda, et al., Phys. Rev. Lett. 108 (2012) 206803.
[26] S. Souma, K. Eto, M. Nomura, K. Nakayama, T. Sato, T. Takahashi, K. Segawa, Y. Ando, Phys. Rev. Lett. 108 (2012) 116801.
[27] T.V. Menshchikova, S.V. Eremeev, E.V. Chulkov, Appl. Surf. Sci. 267 (2013) 1.
[28] S.V. Eremeev, T.V. Menshchikova, I.V. Silkin, M.G. Vergniory, P.M. Echenique, E.V. Chulkov, Phys. Rev. B 91 (2015) 245145.
[29] M.G. Vergniory, T.V. Menshchikova, I.V. Silkin, Yu.M. Koroteev, S.V. Eremeev, E.V. Chulkov, Phys. Rev. B 92 (2015) 045134.
[30] T.B. Zhukova, A.I. Zaslavskii, Sov. Phys. Crystallogr. 16 (1971) 796.
[31] F. Casula, L. Deiana, A. Podda, J. Phys. Condens. Matter 3 (1991) 1461.
[32] K. Adouby, A.A. Toure, G. Kra, et al., C. R. Acad. Sci. Chem. 3 (2000) 51.
[33] O.G. Karpinskii, L.E. Shelimova, M.A. Kretova, E.S. Avilov, V.S. Zemskov, Inorg. Mater. 39 (2003) 240.
[34] F. Ledda, C. Muntoni, S. Serci, L. Pellerito, Chem. Phys. Lett. 134 (1987) 545.
[35] K. Momma, F. Izumi, J. Appl. Crystallogr. 44 (2011) 1272.
[36] E.S. Itskevitch, L.M. Kashirskaya, V.F. Kraidenov, Semiconductors. 31 (1997) 276.
[37] D.A. Polvani, J.F. Meng, N.V. Chandra Shekar, J. Sharp, J.V. Badding, Chem. Mater. 13 (2001) 2068.
[38] S.V. Ovsyannikov, V.V. Shchennikov, G.V. Vorontsov, A.Y. Manakov, A.Y. Likhacheva, V.A. Kulbachinskii, J. Appl. Phys. 104 (2008) 053713.
[39] M.K. Jacobsen, R.S. Kumar, A.L. Cornelius, S.V. Sinogeiken, M.F. Nicol, AIP Conf. Proc. 955 (2007) 171.
[40] R. Vilaplana, D. Santamaría-Pérez, O. Gomis, F.J. Manjón, J. González, A. Segura, A. Muñoz, P. Rodríguez-Hernández, E. Pérez-González, V. Marín-Borrás, V. Muñoz-Sanjose, C. Drasar, V. Kucek, Phys. Rev. B 84 (2011) 184110.
[41] R. Vilaplana, O. Gomis, F.J. Manjón, A. Segura, E. Perez-González, P. Rodríguez-Hernández, A. Muñoz, J. González, V. Marín-Borras, V. Muñoz-Sanjosé, C. Drasar, Kucek, Phys. Rev. B 84 (2011) 104112.
[42] O. Gomis, R. Vilaplana, F.J. Manjón, P. Rodríguez-Hernández, E. Pérez-González, A. Muñoz, V. Kucek, C. Drasar, Phys. Rev. B 84 (2011) 174305.

[43] F.J. Manjón, R. Vilaplana, O. Gomis, E. Pérez-González, D. Santamaría-Pérez, V. Marín-Borrás, A. Segura, J. González, P. Rodríguez-Hernández, A. Muñoz, C. Drasar, V. Kucek, V. Muñoz-Sanjosé, Phys. Stat. Sol. (b) 250 (2013) 669.
[44] A. Nakayama, M. Einaga, Y. Tanabe, S. Nakano, F. Ishikawa, Y. Yamada, High. Pres. Res. 29 (2009) 245.
[45] A. Polian, M. Gauthier, S.M. Souza, D.M. Triches, J. Cardoso de Lima, T.A. Grandi, Phys. Rev. B 83 (2011) 113106.
[46] W. Ibarra-Hernández, M.J. Verstraete, J.Y. Raty, Phys. Rev. B 90 (2014) 245204.
[47] J. Zhang, C. Liu, X. Zhang, F. Ke, Y. Han, G. Peng, Y. Ma, C. Gao, Appl. Phys. Lett. 103 (2013) 052102.
[48] O. Oeckler, M.N. Schneider, F. Fahrnbauer, G. Vaughan, Solid State Sci. 13 (2011) 1157.
[49] F. Fauth, I. Peral, C. Popescu, M. Knapp, Powder Diffr. 28 (2013) 360.
[50] A. Dewaele, P. Loubeyre, M. Mezouar, Phys. Rev. B 70 (2004) 094112.
[51] A.P. Hammersley, S.O. Svensson, M. Hanfland, A.N. Fitch, D. Häusermann, High. Pres. Res. 14 (1996) 235.
[52] T.J.B. Holland, S.A.T. Redfern, Min. Mag. 61 (1997) 65.
[53] W. Kraus, G. Nolze, J. Appl. Crystallogr. 29 (1996) 301.
[54] A.C. Larson, R.B. von Dreele, LANL Report, vol. 86, 2004, p. 748.
[55] B.H. Toby, J. Appl. Crystallogr. 34 (2001) 210.
[56] J.L. van der Paw, Philips Res. Rep. 13 (1958) 1.
[57] H.K. Mao, J. Xu, P.M. Bell, J. Geophys. Res. 91 (1986) 4673.
[58] K. Syassen, High. Pres. Res. 28 (2008) 75.
[59] P. Hohenberg, W. Kohn, Phys. Rev. 136 (1964) 3864.
[60] G. Kresse, J. Hafner, Phys. Rev. B 47 (1993) 558.
[61] G. Kresse, J. Furthmüller, Phys. Rev. B 54 (1996) 11169.
[62] P.E. Blöchl, Phys. Rev. B 50 (1994) 17953.
[63] J.P. Perdew, A. Ruzsinszky, G.I. Csonka, O.A. Vydrow, G.E. Suseria, L.A. Constantin, X. Zhou, K. Burke, Phys. Rev. Lett. 100 (2008) 136406.
[64] F. Birch, J. Appl. Phys. 9 (1938) 279.
[65] L. Zhu, H. Wang, Y. Wang, J. Lv, Y. Ma, Q. Cui, Y. Ma, G. Zou, Phys. Rev. Lett. 106 (2011) 145501.
[66] M. Einaga, A. Ohmura, A. Nakayama, F. Ishikawa, Y. Yamada, S. Nakano, Phys. Rev. B 83 (2011) 092102.
[67] S. Feng, S.M. Li, H.Z. Fu, Comp. Mater. Sci. 82 (2014) 45.
[68] M.D. Frogley, J.L. Sly, D.J. Dunstan, Phys. Rev. B 58 (1998) 12579.
[69] J.A. Sans, F.J. Manjón, A.L.J. Pereira, R. Vilaplana, O. Gomis, A. Segura, A. Muñoz, P. Rodríguez-Hernández, C. Popescu, C. Drasar, P. Ruleova, Phys. Rev. B 93 (2016) 024110.
[70] J.A. Sans, F.J. Manjón, C. Popescu, V.P. Cuenca-Gotor, O. Gomis, A. Muñoz, P. Rodríguez-Hernández, J. Contreras-García, J. Pellicer-Porres, A.L.J. Pereira, D. Santamaría-Pérez, A. Segura, Phys. Rev. B 93 (2016) 054102.
[71] V.V. Kechin, Phys. Rev. B 63 (2001) 045119.
[72] A.B. Garg, V. Vijayakumar, P. Modak, D.M. Gaitonde, R.S. Rao, B. K.Godwal, S.K. Sikka, J. Phys. Condens. Matter 14 (2002) 8795.
[73] G. Xiao, K. Wang, L. Zhu, X. Tan, Y.C. Qiao, K. Yang, Y.M. Ma, B.B. Liu, W.T. Zheng, B. Zou, J. Phys. Chem. C 119 (2015) 3843.
[74] L. Pan, J. Li, D. Berardan, N. Dragoe, J. Solid State Chem. 225 (2015) 168.
[75] A. Segura, V. Panchal, J.F. Sánchez-Royo, V. Marín-Borrás, V. Muñoz-Sanjosé, P. Rodríguez-Hernández, A. Muñoz, E. Pérez-González, F.J. Manjón, J. González, Phys. Rev. B 85 (2012) 195139.
[76] M.K. Jacobsen, S.V. Sinogeiken, R.S. Kumar, A.L. Cornelius, J. Phys. Chem. Sol. 73 (2012) 1154.